Co-pelletization of a zirconium-based metal-organic framework (UiO-66) with polymer nanofibers for improved useable capacity in hydrogen storage

Sonwabo E. Bambalaza [a,b,c], *Henrietta W. Langmi* [d,*], *Robert Mokaya* [e],
Nicholas M. Musyoka [a,**], *Lindiwe E. Khotseng* [b]

[a] *HySA Infrastructure Centre of Competence, Centre for Nanostructures and Advanced Materials (CeNAM), Chemicals Cluster, Council for Scientific and Industrial Research (CSIR), Pretoria 0001, South Africa*
[b] *Faculty of Natural Science, University of the Western Cape, Bellville, Cape Town 7535, South Africa*
[c] *Pyrometallurgy Division, Mintek, 200 Malibongwe Drive, Praegville, Randburg, 2194, South Africa*
[d] *Department of Chemistry, University of Pretoria, Private Bag X20, Hatfield, 0028, South Africa*
[e] *School of Chemistry, University of Nottingham, University Park, Nottingham, NG7 2RD, UK*

HIGHLIGHTS

- Polymer nanofibers incorporated as layers in UiO-66 MOF by co-pelletization.
- Co-pelletization created hierarchical porosity in initially highly microporous MOF.
- Microstructure of composites correlates with useable H_2 storage capacity.
- UiO-66/nanofiber monoliths improved low H_2 useable capacity in UiO-66.

GRAPHICAL ABSTRACT

ARTICLE INFO
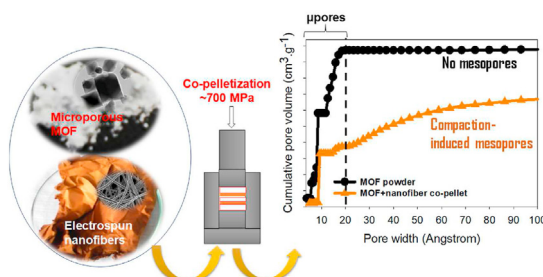
ABSTRACT

We report on a concept of co-pelletization using mechanically robust hydroxylated UiO-66 to develop a metal-organic framework (MOF) monolith that contains 5 wt% electrospun polymer nanofibers, and consists of an architecture with alternating layers of MOF and nanofiber mats. The polymers of choice were the microporous Polymer of Intrinsic Microporosity (PIM-1) and non-porous polyacrylonitrile (PAN). Co-pelletized UiO-66/PIM-1 and UiO-66/PAN monoliths retain no less than 85% of the porosity obtained in pristine powder and pelletized UiO-66. The composition of the pore size distribution in co-pelletized UiO-66/PIM-1 and UiO-66/PAN monoliths is significantly different to that of pristine UiO-66 forms, with pristine UiO-66 forms showing 90% of the pore apertures in the

---

micropore region and both UiO-66/nanofiber monoliths showing a composite micro-mesoporous pore size distribution. The co-pelletized UiO-66/nanofiber monoliths obtained improved useable H_2 capacities in comparison to pristine UiO-66 forms, under isothermal pressure swing conditions. The UiO-66/PIM-1 monolith constitutes the highest gravimetric (*and* volumetric) useable capacities at 2.3 wt% (32 g L^{-1}) in comparison to 1.8 wt% (12 g L^{-1}) and 1.9 wt% (29 g L^{-1}) obtainable in pristine UiO-66 powder and UiO-66 pellet, respectively. The co-pelletized UiO-66/PAN monolith, however, shows a significantly reduced surface area by up to 50% less in comparison to pristine UiO-66, but its pore volume only 13% less in comparison to pristine UiO-66. As a result, total gravimetric H_2 capacity of the co-pelletized UiO-66/PAN monolith is 50% less in comparison to that of pristine UiO-66, but crucially the useable volumetric H_2 capacity is 50% higher for the UiO-66/PAN monolith in comparison to pristine UiO-66 powder. The co-pelletization strategy provides a simple method for generating hierarchical porosity into an initially highly microporous MOF without changing the structure of the MOF through complex chemical modifications. The UiO-66/nanofiber monoliths offer improvements to the typically low H_2 useable capacities in highly microporous MOFs, and open new opportunities towards achieving system-level H_2 storage targets.

Introduction

Hydrogen (H_2) storage in metal-organic frameworks (MOFs) is still an ongoing research challenge, and testing of MOF properties in their shaped forms, e.g. pellets, fibers, or aerogels, is still in its inception despite having significant implications on MOF end use. There has been a rise in the development of strategies to improve MOF properties aimed at system-level H_2 storage applications [1–5]. The development of MOFs has even reached levels where commercialization of MOF materials is a possibility, with Farha et al. [6] highlighting strategies towards commercial viability of MOFs. In H_2 storage applications, efforts to improve the balancing of the useable volumetric and gravimetric H_2 capacities are highlighted by in a recent review by Broom et al. [7]. Which summarizes various strategies such as the synthesis of interpenetrating MOF as a means of improving volumetric H_2 capacity. The benefits of interpenetration were explored by Balderas-Xicohtèncatl et al. [8] where an interpenetrated MOF, CFA-7, achieved twice the volumetric H_2 capacity compared to an equivalent but non-interpenetrated MOF, MFU-4l. The gas uptake of most MOFs can be described by type I sorption isotherms, which means that MOFs typically display useable capacities that are much lower than the total gas (e.g. CH_4, CO_2, or H_2) uptake capacity [9–12]. The US Department of Energy (DOE) targets for H_2

storage systems are exclusively based on the useable/deliverable H_2 capacity of the system (see Table 1), and are, therefore, a big challenge for most promising MOFs that show typical type I H_2 uptake isotherms.

Materials with Type I H_2 uptake isotherms have typically low useable capacities and, therefore, tend to fall far short of the DOE system targets for mobile H_2 storage applications. A variety of so-called flexible MOFs, including "breathing MOFs", have been investigated and do show some promise towards achieving high useable capacities for H_2 storage, but such strategies require the synthesis of new MOFs. A further challenge is that all such modified MOFs would still likely suffer loss of structural integrity when compacted at high pressure to produce pellets [7,14–16]. Flexible MOFs have been shown to exhibit a sigmoidal (S-shaped) type of gas adsorption, whereby the amount of H_2 adsorbed at low pressure is close to zero and adsorption increases at moderate to high pressures [17–19]. The reason is linked to the presence of heterogeneous surface energies as the adsorption sites (pores) are not identical and require adsorption-induced activation at pressures typically greater than 1 bar, as shown in CO_2 and CH_4 uptake (263 K, up to 30 bar) in MIL-53(Al) and its amino-modified analogue, NH_2-MIL-53(Al) [20]. This type of sigmodial adsorption isotherm shows gas uptake is close to zero for low-pressure adsorption and could possibly ensure a useable gas

Table 1 – Summary of a selected US DOE system targets for on-board H_2 storage applications [13].				
Storage parameter	Units	2020	2025	Ultimate
System gravimetric capacity				
Useable gravimetric capacity	kWh/kg (kg H_2/kg system)	1.5 (0.045)	1.8 (0.055)	2.2 (0.065)
System volumetric capacity				
Useable volumetric capacity	kWh/L (kg H_2/L system)	1.0 (0.030)	1.3 (0.040)	1.7 (0.050)
Durability/operability				
Min. deliverable pressure from storage system	bar (abs)	5	5	5
Max. deliverable pressure from storage system	bar (abs)	12	12	12

uptake retained close to 100% of the total/absolute gas uptake. The disadvantage of such pore flexibility is that these MOFs typically have low shear/stress moduli and as a result may undergo crystal changes resulting in reduced porosity (surface area and pore volume) upon compaction at high pressure during pelletization [15,16,21,22]. As shown in previous studies [23,24], pelletization is an important fabrication method that can improve the volumetric H_2 capacity of MOFs due to improved packing density. In our previous studies [25,26], we have shown that the hydroxylated form of UiO-66 can be pelletized at very high pressure (ca. 700 MPa) to improve volumetric H_2 capacity, but importantly without compromising its gravimetric H_2 capacity. The results showed great promise towards balancing the volumetric and gravimetric H_2 capacities within a single MOF-based H_2 storage material, however, UiO-66 contains a highly microporous framework composed of no less than 90% narrow pore apertures (<10 Å). The highly microporous nature of UiO-66 becomes problematic when considering the useable/deliverable volumetric and gravimetric H_2 capacities. Due to this highly homogeneous and microporous structure of pristine and defect-free UiO-66, H_2 adsorption in UiO-66 is largely governed by Henry's constant and the micropore filling mechanism which are dominant at low-pressure adsorption conditions [27]. In addition, UiO-66 is most commonly synthesized containing some level of defects in its crystal structure, especially under acid-modulated solvothermal conditions. The presence of defects, such as missing linker sites, potentially create open metal sites that exhibit enhanced H_2 adsorption due to the strong interaction of H_2 and metal cation cluster(s) [28]. The combination of defects and narrow pore apertures renders typical Type I H_2 sorption isotherms in UiO-66, meaning there is a greater low-pressure adsorption rate and quantity adsorbed (P < 5 bar), but significantly lower at higher pressures. The result is a very low useable H_2 uptake/capacity, typically ca. 50% of the total H_2 uptake measured for UiO-66 powders [26].

There have been efforts to improve the useable H_2 capacities of highly microporous adsorbents such as UiO-66. Simulation studies by Tsivion et al. [29] predict that the incorporation of catechol linkers metalated with alkali-earth metal ions such as Ca^{2+} and Mg^{2+} may induce the creation of open metal sites in the UiO-66 framework. This is predicted to improve not only the room temperature H_2 uptake of the functionalized UiO-66 compared to pristine UiO-66, but importantly predicted to improve the useable volumetric H_2 capacity from ca. 10 g L^{-1} to ca. 30 g L^{-1}. Experimental studies by Liu et al. [30] have shown that a hierarchically porous adsorbent, consisting of a combination of micropores and mesopores, as one of the successful strategies at improving the useable gas uptake of physisorbed gases such as carbon dioxide (CO_2) and methane (CH_4), mainly due to the extension of the pore structure afforded via the creation of mesopores into an initially microporous adsorbent. In addition to extending the porosity of an initially microporous adsorbent, their study also shows the presence of mesopores to increase the rate of gas diffusion during adsorption.

The current study attempts to improve the useable/deliverable H_2 capacity of a mechanically robust and highly microporous MOF, i.e., UiO-66, via composite formation (via co-pelletization) with electrospun nanofibers in order to possibly impart additional porosity in the resultant monolithic structure.

A variety of MOFs, ranging from zirconium-, iron-, chromium-, and copper-based MOFs, have been successfully electrospun with polymers such as polyacrylonitrile (PAN), polyvinylidene fluoride (PVDF), Poly-L-lactide (PLL) and polystyrene (PS), among others. The advantage of producing MOF/polymer monoliths is that they can be obtained as fibrous membranes that are useable in applications such as gas separation, chemical sensors, water purification and as polymer-based binders in shaping of powdered solid-state adsorbents [31–34]. The disadvantage of incorporating MOFs in nanofibers is the tendency for the MOF/nanofiber monoliths to show compromised properties compared to the pristine MOF powders. This arises from limitations of the electrospinning process, such as the limits on the amount of MOF powder that can be loaded onto an electrospinnable MOF/polymer solution [35]. In addition to electrospinning of MOF/polymer solutions, porous polymers such as polymers of intrinsic microporosity (PIMs) have also been shown to be electrospinnable [36]. The advantage of PIMs is that they possess permanently microporous structure that is not lost upon processing them into powders, nanofibers, or thin films [37]. The H_2 storage capacity of porous polymers, including MOF/polymer nanofibers, is known to be comparable to that for pristine MOF powders [33,35]. In this study, we introduce a concept of co-pelletization of a microporous MOF, namely UiO-66, with electrospun nanofibers to obtain a MOF-based monolith with hierarchical porosity, i.e., a mixture of pore apertures in the micropore and mesopore range. In previous studies, MOFs and MOF monoliths with hierarchical porosity have been developed via chemical modifications such as sol-gel [4,8,38–40] and functionalization [41–44]. In the proposed co-pelletization strategy we aim to combine two simple fabrication techniques, namely compaction/pelletization and electrospinning, to generate mesopores into a highly microporous MOF via physical mixing of MOF powder with nanofibers. The attraction of porous solids with hierarchical porosity is that they can show combinations of types of gas adsorption isotherms. For example, a micro-mesoporous material can show Type I adsorption at low pressure and also Type II or Type III adsorption at higher pressures [45–48]. This could improve the deliverable/useable capacity of the adsorbed gas, which has significant implications in system-level H_2 storage applications [8]. This study, therefore, exploits the mechanically robust nature of the hydroxylated UiO-66 form, as reported in our previous studies [25,26], in combination with electrospun nanofibers, in an attempt to obtain a UiO-66/nanofiber monolith with improved deliverable/usable H_2 capacity compared to pristine UiO-66 forms.

Experimental

Reagents

Zirconium tetrachloride ($ZrCl_4$, Sigma Aldrich, 9.5%), 1,4-Benzenedicarboxylic acid (BDC, Sigma Aldrich, 98%), N,N-dimethylformamide (DMF, Sigma Aldrich, 99.8%), formic acid (HCOOH, Sigma Aldrich, 95%) and dried acetone (Sigma

Aldrich, 99.8%) were purchased and used without further purification. Polyacrylonitrile (PAN, M_w = 150 000 Da, Sigma Aldrich), Polymethylmethacrylate (PMMA, M_w = 120 000 Da, Sigma Aldrich), and PIM-1 (PIM = Polymers of Intrinsic Microporosity) were the choice of polymers for electrospinning in this work and were also used without further purification after their purchase. The PIM-1 was used in as synthesized form according to Budd et al. [49].

Preparation of electrospun PIM-1, PMMA@PAN, and UiO-66/PMMA@PAN nanofibers

The UiO-66 MOF was synthesized as reported in our previous study using an acid-modulated solvothermal crystal growth method [25,26].

Electrospun PIM-1 nanofibers were prepared by dissolving 0.6 g of PIM-1 granules in a 7:3 v/v tetrachloroethane (TCE):-tetrahydrofuran (THF) solvent mixture, which was then fed through a syringe pump at a flow rate of 3 mL h^{-1} and subjected to 16 kV applied voltage. The PIM-1 nanofibers were collected on an aluminum foil screen at a distance of 15 cm from the needle tip.

The preparation of PMMA@PAN and UiO-66/PMMA@PAN nanofibers was carried out using a coaxial electrospinning method where two separate solutions, dissolved or dispersed in DMF, were fed through an automated syringe pump system, through a concentric needle, at a flow rate of 1.8 mL h^{-1} (Fig. S1). The "@" and "/" denote a core-shell and physical mixture, respectively. The optimum polymer concentrations for PAN and PMMA were 8 wt% (0.755 g in 10 mL DMF) and 25 wt% (2.36 g in 10 mL DMF), respectively. An applied voltage of 11 kV was used for both the pristine PIM-1 and co-electrospun UiO-66/PMMA@PAN nanofibers, the latter containing a UiO-66 loading of 20 wt% prior to electrospinning. The polymer/MOF solution/emulsion were prepared to a fixed volume of 10 mL, hence the amount of UiO-66 powder in the PAN solution was 0.151 g and 0.472 g in the PMMA solution. The core-shell PMMA@PAN and UiO-66/PMMA@PAN nanofibers were further subjected to treatment with acetone in order to selectively remove PMMA without affecting the PAN and UiO-66 components. The PMMA removal step was conducted by soaking the nanofibers in excess acetone for 10 min, followed by severally washing in fresh acetone aliquots.

Co-pelletization of UiO-66/PAN nanofiber monoliths

The UiO-66 powder and UiO-66/nanofiber were co-pelletized as alternating MOF-nanofiber-MOF-nanofiber-MOF layers (ESI, Fig. S2) using a manual hydraulic press at an applied force of 9 metric tonnes (665 MPa), with each sample maintained at that force for 5 min. The co-pelletized monoliths consist of 5 wt% nanofiber, which is divided into equal parts (i.e. 2.5 wt%) for each nanofiber layer. In Fig. 1, a schematic demonstrates the ratios of nanofiber to MOF powder and compression pressure used during the preparation of the monoliths.

Characterization

Powder X-ray diffraction (PXRD) patterns of pristine and composite materials were collected within the 2θ range of 3° − 60°

using a Rigaku Ultima IV X-ray diffractometer with CBO technology using Ni-filtered Cu-Kα radiation of 0.154 nm (40 kV, 30 mA) at a scanning speed of 5°s^{-1}. The surface morphology was analysed using an Auriga cobra Focused-Ion Beam Scanning Electron Microscope (FIB-SEM) where each sample was mounted on a carbon tape and coated with carbon (where necessary) prior to analysis. Nitrogen sorption isotherms at 77 K were obtained on a Micromeritics 3-Flex sorptometer. Ultra-high purity grade (99.999%) nitrogen was used, and each sample was degassed on a Micromeritics Smart VacPrep under vacuum (up to 10^{-7} bar) at 80 °C for 16−32 h prior to analysis. Pore size distribution curves were obtained using the Non-Local Density Functional Theory (NLDFT) model. The thermal stability of pristine and composite materials was assessed with a thermogravimetric analyzer (TGA) (Mettler, Toledo, TGA/SDTA 851e) on degassed samples. For each run, ca. 10 mg of the sample was heated up to 1000 °C at 10 °C min^{-1} and 100 mL min^{-1} air flow. Excess hydrogen uptake measurements were carried out using a Hiden Isochema Intelligent Gravimetric analyzer, in the pressure range of 0−100 bar at 77 K using 6.0 grade H$_2$ (99.9999%), additionally purified through a molecular sieve filter. The measured excess H$_2$ uptake data was corrected for buoyancy effects by accurately measuring the skeletal density of each sample using helium (He) pycnometry (Micromeritics AccuPy II 1340 model). The low-pressure adsorption (P < 10 bar) measurements were allowed 30 min equilibration time prior to measurement of a higher pressure. For the moderate to high pressure adsorption (10 < P < 100), the equilibration time was 10 min at each pressure. The total/absolute gravimetric and volumetric H$_2$ capacities were calculated as reported in our previous work [25,26].

Results and discussion

Electrospinning of PMMA and PAN for the incorporation of UiO-66 crystals

This section reports on the preparation of polymer nanofibers and MOF/nanofiber monoliths via electrospinning. The PIM-1 nanofibers were prepared by conventional single-nozzle electrospinning, whilst the PAN-based nanofibers were prepared using a co-axial electrospinning technique, which generates nanofiber with a core-shell morphology. The as-spun core-shell PMMA@PAN and UiO-66/PMMA@PAN nanofibers were then subjected to treatment with acetone in order to selectively remove the PMMA component and possibly result in the improvement of the UiO-66 loading without affecting the PAN component of the nanofibers. A combination of electron microscopy imaging and chemical analysis techniques are used to elucidate the effect of solvent-based selective core removal from the co-electrospun nanofibers.

The results in Fig. 2a and b as well as Fig. S3 (ESI) show the SEM and TEM images for microstructural analysis of the nanofibers. In Fig. 2a it can be seen that the co-electrospinning of PMMA and PAN polymers produced nanofiber with a core-shell morphology containing both PMMA and PAN as confirmed by FTIR spectra (ESI, Fig. S4). Upon immersion of the PMMA@PAN nanofibers in acetone, the FTIR spectra and TGA profile of the remaining nanofibers show that PMMA is
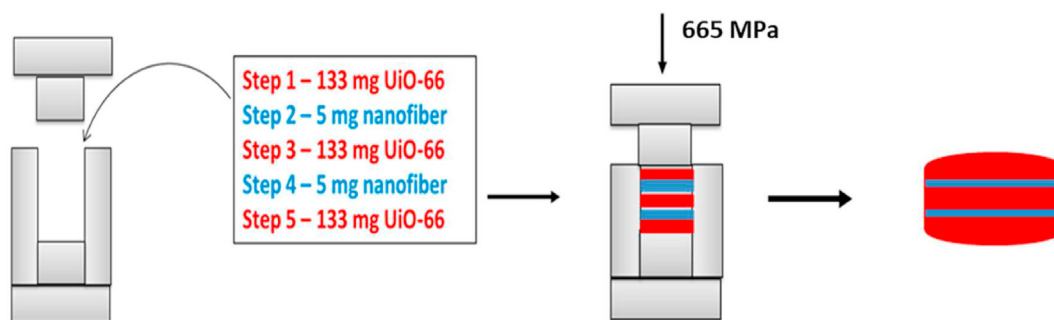
Fig. 1 — Schematic representation of the co-pelletization of UiO-66 with electrospun nanofibers.
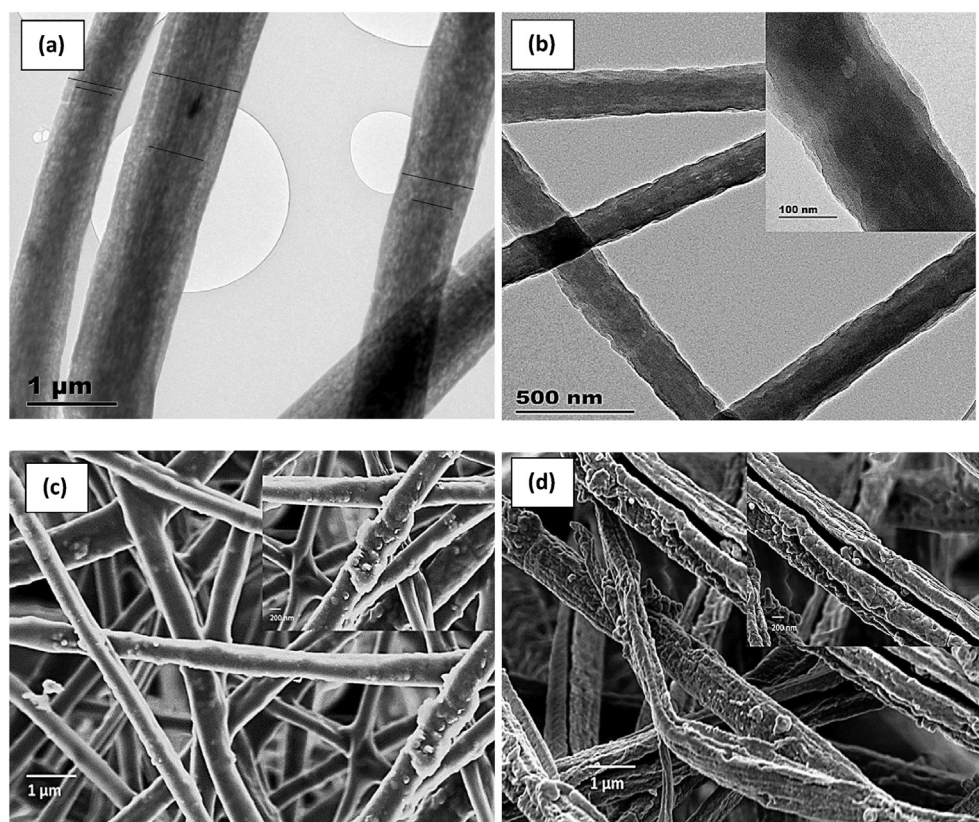

Fig. 2 — Electron microscopy images of co-electrospun nanofibers in the presence and absence of MOF crystals: (a) TEM image of as-spun PMMA@PAN nanofibers; (b) TEM image of PMMA@PAN nanofiber after removal of PMMA with acetone; (c) SEM image of as-spun UiO-66/PMMA@PAN nanofibers, and (d) SEM image of UiO-66/PAN-(AR) nanofibers after removal of PMMA via immersion in acetone.

completely dissolved, thereby leaving behind only PAN nanofibers (Fig. 2b and ESI, Figs. S4 and S5). The incorporation of UiO-66 crystals into PMMA@PAN nanofibers is confirmed by PXRD, FTIR, and TGA analyses (ESI, Figs. S6-S9). Fig. 2c also shows that the UiO-66 crystals are encapsulated within the PMMA and PAN polymer matrix. Following the immersion of the UiO-66/PMMA@PAN nanofibers in acetone, the FTIR spectrum (ESI, Fig. S7) of the resultant composite shows only UiO-66 and PAN vibrational bands, a sign that PMMA is successfully removed from the core-shell nanofiber composite. The resultant UiO-66/PAN-(AR) nanofibers (AR = after removal), however, exhibit a high degree of physical damage

that is not observed in the acetone-treated nanofibers with no UiO-66 (Fig. 2b and d). It is, however, noticeable that the resultant PAN nanofibers from the latter show reduced fiber diameters and become flattened following the removal of PMMA (Fig. 2b). It can be seen that in the presence of UiO-66 crystals, this reduction in diameter and flattening possibly leads to the observed damage (grooves) and explains the rupturing observed in the UiO-66/PAN-(AR) nanofibers (Fig. 2d).

The removal of PMMA from the UiO-66/PMMA@PAN nanofibers could be expected to increase the UiO-66 loading onto the resultant PAN nanofibers and possibly result in

improved surface area and pore volume. This hypothesis may be true assuming that complete retention of the UiO-66 crystals within the PAN matrix and no weight loss in PAN are observed after selective PMMA removal, then the UiO-66/PAN-(AR) nanofibers would contain an improved UiO-66 loading of 83 wt% with respect to the mass of PAN. Since the UiO-66/nanofiber monoliths are predominantly a physical mixture of UiO-66 crystals embedded in the polymer matrix, and with little to no evidence of chemical interactions in the UiO-66/nanofiber monoliths, then the percentage increase in the UiO-66 loading would be expected to correlate to an improvement of textural properties (pore volume and surface area) by a factor of four (4), due to the UiO-66 loading increasing from 20 wt% to ca. 80 wt% post-PMMA removal. Any deviations from the above-mentioned assumptions could compromise these expected outcomes. The aforementioned assumptions, however, do not take into account the effects of pore blocking that is notoriously observed in polymer/MOF composite types, whereby the result is a compromise in some of the MOF's textural properties such as surface area and pore volume [33,35]. By considering the effects of pore blocking, the textural properties of UiO-66/PAN-(AR) nanofibers may not fully reach the hypothesized improvement of a factor four (4) increase in the surface area and pore volume, but are expected to improve significantly in comparison to the UiO-66/PMMA@PAN nanofibers as the latter would experience a higher degree of pore blocking due to the presence of the PMMA nanofibers.

Textural properties and H_2 storage of free-standing PIM-1 and PAN-based nanofibers

Indeed, it can be seen in Fig. 3 that the N_2 sorption isotherms obtained for the UiO-66/PMMA@PAN nanofibers show lower adsorption capacity in comparison to the UiO-66/PAN-(AR) nanofibers. Since there was no addition of UiO-66 crystals after PMMA removal, it can be assumed that the observed
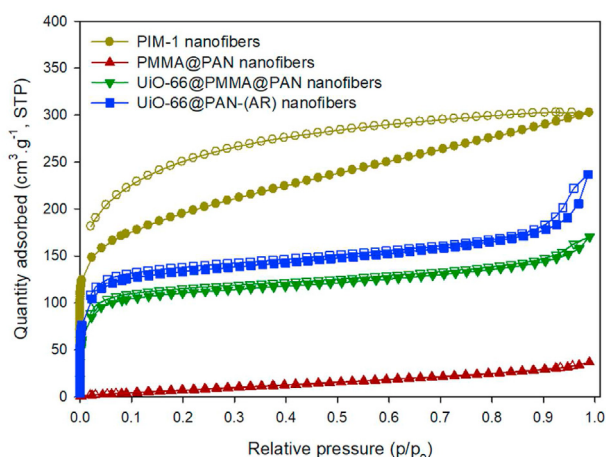

Fig. 3 − N_2 adsorption isotherms at 77 K obtained for pristine and composite polymer nanofibers: PIM-1, PAN, core-shell UiO-66/PMMA@PAN, and UiO-66/PAN (AR) after removal of the PMMA core. Desorption isotherms are shown as open symbols.

improvement in the N_2 adsorption capacity is due to an increase in the UiO-66 loading onto the resultant UiO-66/PAN-(AR) nanofibers with surface area of 421 and 508 m2 g^{-1} for UiO-66/PMMA@PAN and UiO-66/PAN-(AR), respectively (Table 2). This means, the surface area of the UiO-66/PAN-(AR) only show an improvement of 21% in comparison to UiO-66/PMMA@PAN nanofibers. This improvement is much lower than the expected 60% increase in UiO-66 loading post-PMMA removal. This can only mean the UiO-66 loading in UiO-66/PAN-(AR) was much lower than the expected ca. 80 wt%. Some of the factors that may influence the surface area of the composite may also originate from potential pore blocking in UiO-66 due to the presence of polymer chains in the composite. The results in Fig. 2d also show clear physical damage to the UiO-66/PAN-(AR) nanofibers, which could possibly result in some UiO-66 crystals leaching out of the PAN nanofibers through such grooves.

The N_2 sorption isotherms observed for PMMA@PAN nanofibers show that the non-porous nature of PMMA and PAN polymers results in typical type III adsorption isotherms with no hysteresis. The small amount of adsorption observable at high relative pressure (p/p$_o$) is attributed to multilayer adsorption of N_2 molecules at 77 K [48,52,53]. The N_2 adsorption isotherm of PIM-1 nanofibers shows type I with typical high adsorption at low relative pressure (p/p$_o$ < 0.05), showing a highly microporous pore structure in PIM-1. The presence of a large hysteresis loop, in the desorption isotherm, down to a relative pressure (p/p$_o$) of ~0.2 is also observed and according to the International Union of Pure and Applied Chemistry (IUPAC) classification of gas sorption isotherms, hysteresis loops typically arise in materials that contain mesopores [51]. Studies have shown that the micropores in PIM-1 can undergo adsorption-induced changes during gas uptake, possibly resulting in mesopore-sized apertures at high relative pressure [52]. The hysteresis loop was also observed over a large pressure range, a phenomenon that commonly indicates interconnected pores consisting of different shapes such as ink-bottle shaped pores. Such pore shapes have been shown to delay desorption of gas molecules from condensate within the pores [51].

The experimental results in Fig. 4, show the pore structure of PIM-1 to consist of pore apertures in the micropore region, at ca. 6, 8, and 13 Å in diameter and mesopores of about 50−100 Å in diameter. The cumulative plot in Fig. 4c confirms the sharp pore-filling in PIM-1 at about 6−10 Å followed by a gradual filling of pores with diameters from 20 to 100 Å, the latter being attributed to the adsorption-induced swelling of the pores. In the PAN-based UiO-66/nanofiber monoliths, the pore size distributions of both UiO-66/PMMA@PAN and UiO-66/PAN-(AR) nanofibers, show pore apertures of about 12 and 16 Å in the micropore region. These pore apertures are intrinsic to the UiO-66 structure as the PAN nanofibers are non-porous. It is noticeable that a pore aperture of 6 Å is present in UiO-66/PAN-(AR) nanofibers and not observable in UiO-66/PMMA@PAN nanofibers. This provides some evidence of pore blocking that may be predominant in the as-spun UiO-66/PMMA@PAN nanofibers (prior to selective PMMA removal). It is further noted that there are mesopores in UiO-66/PAN-(AR) nanofibers, with a diameter of about 500 Å, which possibly explain the 500 Å wide grooves (Fig. 2d) present on the

Table 2 – Summary of the BET surface area, pore volume, and H_2 uptake for pristine and composite polymer nanofibers.

Sample	Surface area $(m^2 \cdot g^{-1})$[a]	Pore volume $(cm^3 \cdot g^{-1})$[b]	Excess H_2 uptake (wt%)	Total H_2 uptake at 5 bar (wt%)	Total H_2 uptake at 100 bar (wt%)	Useable H_2 capacity (wt%)[c]
PIM-1	712 (290)	0.47 (0.12)	1.9	1.9	2.7	0.8
PAN	26 (−)	0.06 (−)	−	−	−	−
UiO-66/ PMMA@PAN	421 (300)	0.26 (0.12)	−	−	−	−
UiO-66/PAN-(AR)	508 (361)	0.37 (0.14)	1.0	1.0	1.1	0.1

(−) Showed negative values for micropore surface area and volume.
[a] Values in parentheses represent the micropore surface area.
[b] Values in parentheses represent the micropore volume.
[c] Values calculated from the difference between total H_2 uptake at 100 bar (adsorption) and 5 bar (desorption).
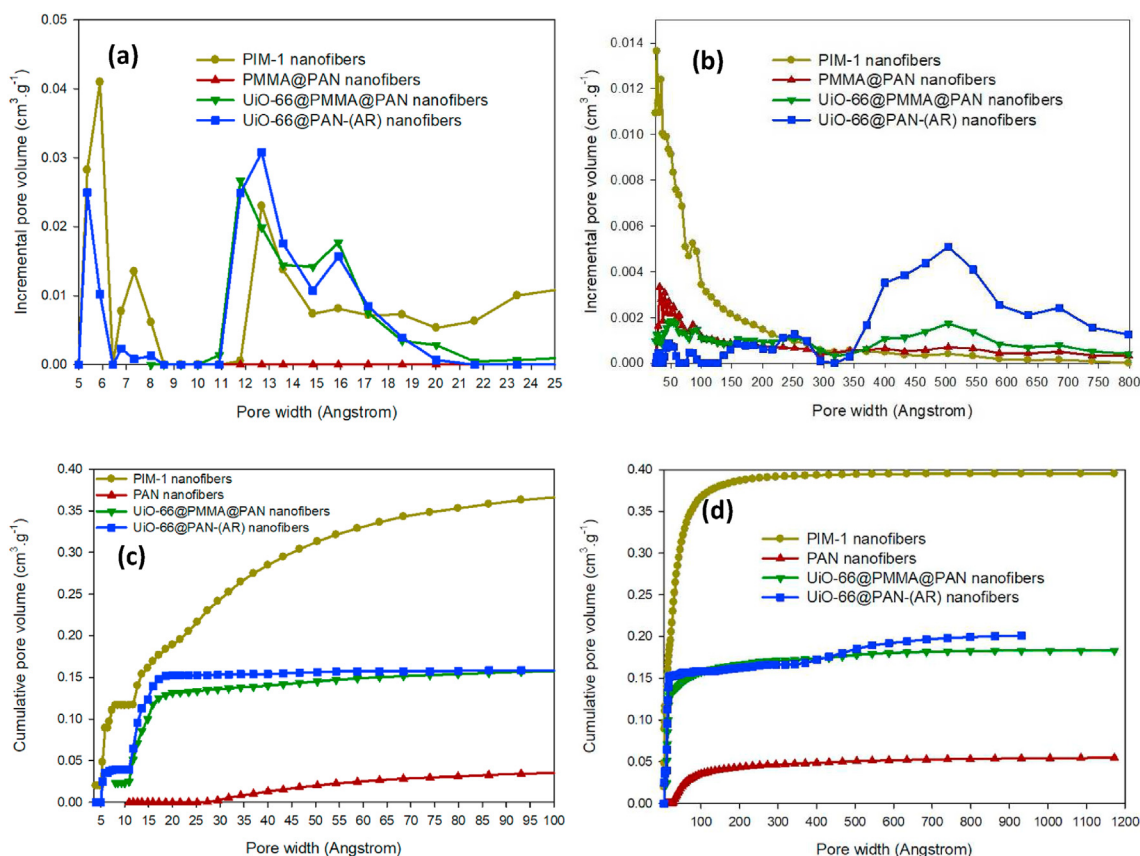

Fig. 4 – NLDFT pore size distribution curves at 77 K obtained for pristine and composite polymer nanofibers: PIM-1, PAN, core-shell UiO-66/PMMA@PAN, and UiO-66/PAN after removal of the PMMA core. (a)–(b) NLDFT incremental pore volume, and (c)–(d) NLDFT cumulative pore volume.

surface of the UiO-66/PAN-(AR) nanofibers, after PMMA removal. Due to the effects of pore blocking by the remaining PAN polymer chains, and physical damage to the UiO-66/PAN-(AR) nanofibers, the initially assumed four-fold theoretical increase in the UiO-66 loading after the removal of PMMA is therefore not achievable under the specified conditions. The results, however, do show clear indication of the reduced pore blocking effects after PMMA removal and subsequent improvements in the surface area and pore volume.

Fig. 5 shows that the hydrogen sorption isotherms (total uptake) obtained for free-standing PIM-1 and UiO-66/PAN-(AR)

nanofibers both exhibit reversible Type I isotherms with maximum excess H_2 uptake of 1.9 wt% and 1.0 wt% for PIM-1 and UiO-66/PAN (AR) nanofibers, respectively. The total/absolute H_2 uptake, at 100 bar, for PIM-1 and UiO-66/PAN-(AR) nanofibers were 2.7 wt% and 1.1 wt%, respectively, with the respective usable H_2 capacities only reaching 35% and 10%, respectively, of their total H_2 uptake.

The observed low useable capacities are typical for highly microporous materials that show Type I sorption isotherms, and indicate that co-electrospinning of UiO-66 with non-porous PAN nanofibers maintains the Type I gas adsorption
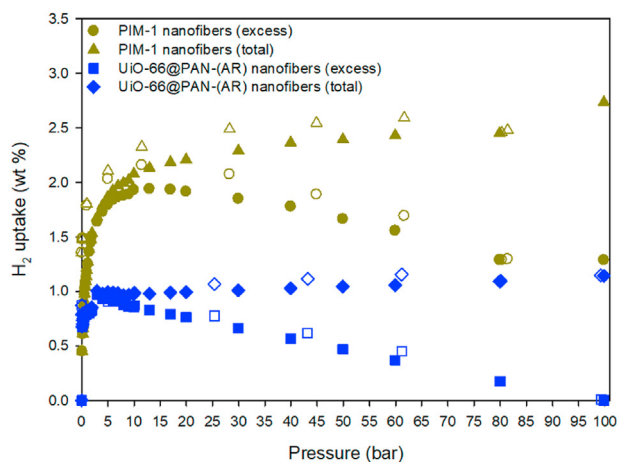
Fig. 5 – H_2 sorption isotherms obtained at 77 K and up to 100 bar, obtained for free-standing PIM-1 and UiO-66/PAN-(AR) nanofibers. The open symbols represent the desorption isotherms.

Fig. 6 – N_2 sorption isotherms at 77 K obtained for pristine UiO-66 and co-pelletized UiO-66/nanofiber monoliths. The open symbols represent the desorption isotherms.

behavior of pristine UiO-66 for UiO-66/PAN nanofibers with at least 20 wt% UiO-66 loading. We, therefore, investigated the strategy of co-pelletization in order to generate hierarchical porosity in a UiO-66/nanofiber composite such that low-pressure H_2 uptake (P ≤ 5 bar) is reduced while maintaining a high or increasing H_2 uptake at moderate to high pressure (i.e., 20–100 bar).

Textural properties and H_2 storage of pristine UiO-66 in comparison to co-pelletized UiO-66/nanofiber monoliths

The proposed co-pelletization strategy involves the simultaneous pelletization of UiO-66 powder and electrospun nanofibers, PIM-1 and UiO-66/PAN-(AR), to form alternating UiO-66-nanofiber layers as shown in cross-sectional SEM images (ESI, Fig. S2). In Fig. S2(ESI), the UiO-66 powder and nanofiber layers are distinctly clear from one another and there are clear differences in the morphology of the layers. In the UiO-66 layers, there is evidence of a high degree of densification of the powder particles with no evidence of individual crystals, but the nanofiber layers show retention of the network or nanofiber mat morphology typically observed for the free-standing three dimensional fiber mats. In our previous studies [25,26], we showed that pelletization of UiO-66 at ca. 700 MPa does not compromise its crystal structure, and hence the densification observed (ESI, Fig. S2) only represents highly packed UiO-66 particles and possibly reduced grain boundaries amongst the crystals after pelletization at 700 MPa.

In Fig. 6 it can be seen that the textural properties of the co-pelletized UiO-66+PIM-1 and UiO-66+UiO-66/PAN-(AR) monoliths show some distinct differences in comparison to those of pristine UiO-66 powder and pellet. In Fig. 6, the N_2 sorption isotherms for pristine UiO-66 show typical reversible Type I isotherms with no evidence of hysteresis, as expected for the highly microporous UiO-66 [53–55]. The UiO-66+PIM-1 monolith shows Type I isotherm similar to UiO-66 pellet due to the synergic contribution of micropores present in both
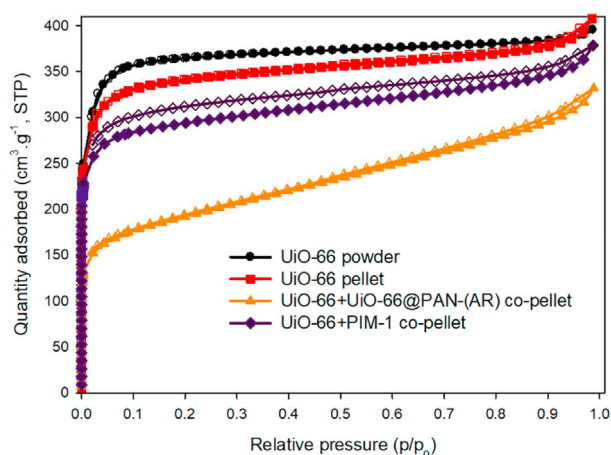
PIM-1 nanofibers and UiO-66 crystals. In addition, there is a clear hysteresis loop from p/p_o ~1 to 0.1, as previously shown in free-standing PIM-1 nanofibers (Fig. 3). The observation of a large hysteresis loop on the UiO-66+PIM-1 monolith could be an indication for the PIM-1 nanofibers retaining their adsorption-induced pore swelling observed in free-standing PIM-1 nanofibers, which consequently suggests that the PIM-1 nanofiber mat network structure is also maintained within the monolith.

The incorporation of the non-porous PAN-based nanofibers are found to give significantly different isotherms. In Fig. 6, the N_2 sorption isotherm obtained for UiO-66+UiO-66/PAN-(AR) monolith shows significantly lower adsorption at low relative pressure (p/p_o < 0.1) compared to pristine UiO-66 forms and UiO-66+PIM-1 monolith, however, with increasing N_2 adsorption at p/p_o close to 1.0. The observed isotherm shape for the UiO-66+UiO-66/PAN-(AR) monolith is a composite type I/type III isotherm, which indicates a hierarchically porous structure. Indeed, in Fig. 3, the free-standing as-spun PMMA@PAN nanofibers show a reversible Type III isotherm, and both powder and pelletized pristine UiO-66 forms show Type I isotherms (Fig. 6). The observed composite isotherm in the UiO-66+UiO-66/PAN-(AR) monolith suggests strong correlations to the contributions of Type III adsorption character from the PAN nanofibers, a phenomenon that was clearly not observed in the N_2 sorption isotherm of free-standing UiO-66/PMMA@PAN and UiO-66/PAN-(AR) nanofibers (Fig. 3). The significantly reduced low-pressure adsorption (at p/p_o < 0.1) in the UiO-66+UiO-66/PAN-(AR) monolith in comparison to pristine UiO-66, coupled to the increasing adsorption at moderate to high relative pressure (p/p_o > 0.1), is an indication of the presence of a hierarchically porous/micro-mesoporous monolith structure. To confirm the composition of the pore structure of the samples, the pore size distributions of each sample is given in Fig. 7.

The incremental and cumulative pore size distributions in Fig. 7a–d clearly show pore apertures, for both UiO-66 powder and pellet, to predominantly occur in the micropore region (<20 Å), with negligible amounts of meso- or macropore
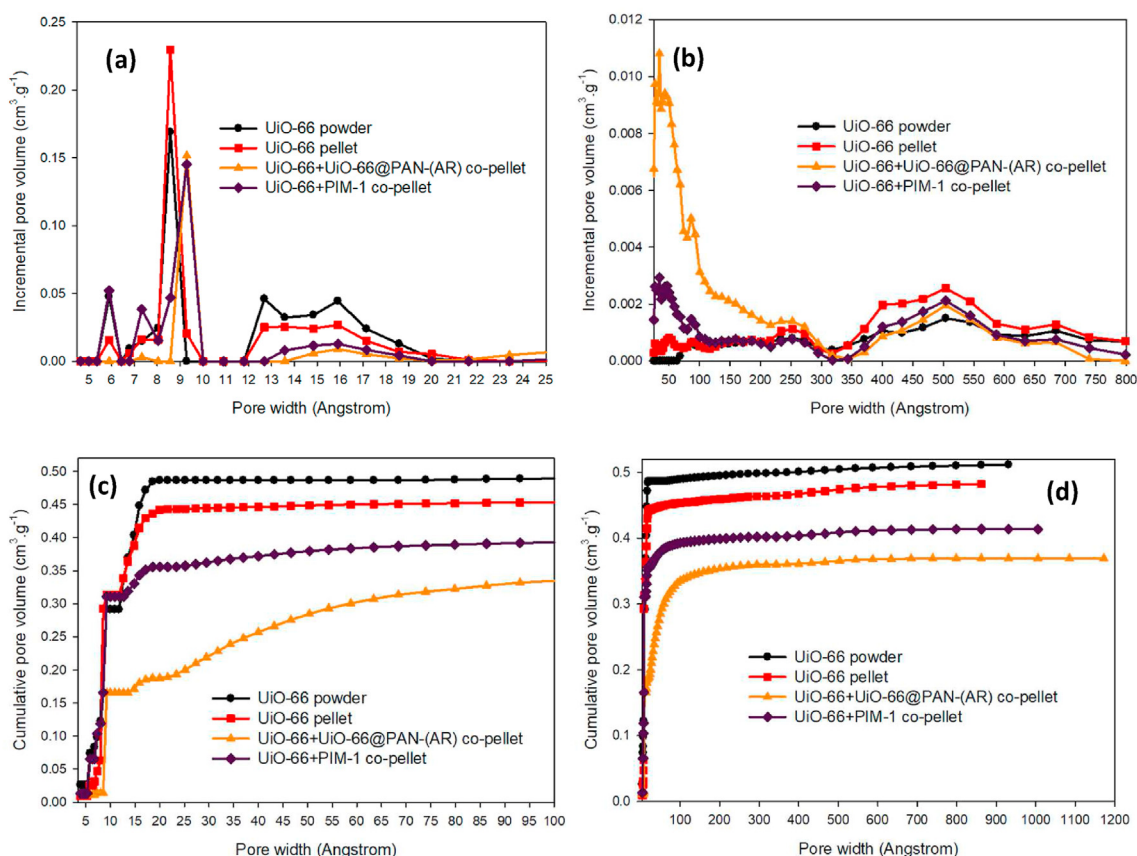
Fig. 7 – NLDFT pore size distribution curves at 77 K obtained for pristine UiO-66 and UiO-66/nanofiber monoliths: UiO-66 powder, UiO-66 pellet, UiO-66+PIM-1 monolith, and UiO-66+UiO-66/PAN (AR). (a)–(b) NLDFT incremental pore volume, and (c)–(d) NLDFT cumulative pore volume.

apertures. In Fig. 7a and b, the UiO-66+nanofiber monoliths both show the same pore apertures as pristine UiO-66 in the micropore region, although the pore volumes is reduced for pores 12–20 Å wide, suggesting some degree of pore blocking possibly via the crystal-nanofiber interactions. In addition, there is clear evidence of mesopores of ca. 50 Å in size for both the UiO-66+PIM-1 and UiO-66+UiO-66/PAN-(AR) monoliths. Further confirmation of mesopores in the monoliths can be seen in the cumulative distribution curves (Fig. 7c and d), which show gradual pore filling within pore widths ranging from 25 to 100 Å. The possibility of mesopore formation can be contemplated by considering the packing of UiO-66 particles/crystals within the nanofiber layers in the monoliths (Fig. S2, ESI). In the layers, it can be assumed that the crystal-crystal packing and densification is reduced due to the presence of nanofibers in comparison to the highly densified UiO-66 layers (Fig. S2, ESI). The reduced densification and crystal-nanofiber surface interactions may possibly result in 'new' porosity generated at the crystal-nanofiber surface interfaces resulting in the observed mesopores. The mesopore filling, in Fig. 7c and d, is also most prominent in the UiO-66+UiO-66/PAN-(AR) monolith, while a lower amount is observable in the UiO-66+PIM-1 monolith. In Fig. 4, however, there was a significant contribution of mesopores, between 50 and 100 Å, in free-standing PIM-1 nanofibers that were not observed in free-standing UiO-66/PAN-(AR) nanofibers. The presence of the

50 Å wide mesopores in the UiO-66+UiO-66/PAN-(AR) monolith can, therefore, be attributed to being a direct result of the co-pelletization strategy of UiO-66 powder with the UiO-66/PAN-(AR) nanofibers.

The results suggest that the incorporation of UiO-66/PAN-(AR) nanofibers via co-pelletization induces the formation of mesopores previously not present in the as-spun nanofibers and in pristine UiO-66. In Table 3 it is shown that even though the UiO-66+UiO-66/PAN-(AR) monolith has a surface area 50% lower than that of UiO-66 powder, its pore volume was only 15% lower. The micropore volume of UiO-66+UiO-66/PAN-(AR) monolith is ca. 27% of its total pore volume, showing considerable contribution of the mesopores to the total pore volume of the monolith. The micropore volume of pristine UiO-66 powder and UiO-66 pellet are in excess of 70% of their respective total pore volumes, illustrating the highly microporous character of pristine UiO-66. The PIM-1 nanofibers consist of micropores in their base polymer structure, and as shown in Fig. 4 and Table 2, the degree of microporosity and thus micropore volume in UiO-66+PIM-1 monolith is considerably higher in comparison to that of the UiO-66+UiO-66/PAN-(AR) monolith, meaning the ratio of mesopores:micropores in UiO-66+PIM-1 is lesser in comparison to that of UiO-66+UiO-66/PAN-(AR) monolith.

The results demonstrated in the N_2 sorption isotherms (Fig. 6 and Table 3) and pore size distribution curves (Fig. 7)

Table 3 — Summary of the BET report and packing/bulk densities obtained for pristine UiO-66 and co-pelletized UiO-66/nanofiber monoliths.

Sample	BET surface area[a] ($m^2 g^{-1}$)	Pore volume[b] ($cm^3 g^{-1}$)	Packing density[c] ($g cm^{-3}$)	Ref.
UiO-66 powder	1413 (1260, 89%)	0.61 (0.50, 82%)	0.65[d]	[23]
UiO-66 pellet	1300 (1091, 84%)	0.60 (0.44, 73%)	1.52	[23]
UiO-66+PIM-1 co-pellet	1113 (902, 81%)	0.59 (0.36, 61%)	1.41	This work
UiO-66 + UiO66/PAN-(AR) co-pellet	702 (350, 50%)	0.52 (0.14, 27%)	1.38	This work

[a] Values in parenthesis are micropore surface area and percentage micropore surface area of the total surface area.
[b] Values in parenthesis are micropore volume and percentage micropore of the total pore volume.
[c] Tapped for UiO-66 powder and pellet dimensions for UiO-66 pellet/co-pellets.
[d] Measured from the tapped mass of 1 mL UiO-66 powder (degassed) in a 5 mL measuring cylinder.

indicate a clear engineering of mesopores through co-pelletization of UiO-66 with PIM-1 and PAN-based polymer nanofibers, thereby inducing hierarchical porosity in the UiO-66/nanofiber monoliths in comparison to the predominantly microporous UiO-66 pristine forms. In Figs. 8 and 9, and Table 4, the H_2 uptake of pristine UiO-66 powder and pellet are compared to the monoliths of UiO-66+PIM-1 and UiO-66+UiO-66/PAN-(AR) in order to investigate the possible effect of hierarchical porosity on hydrogen sorption.

The gravimetric H_2 isotherms in Fig. 8 show both the pristine UiO-66 forms and UiO-66+nanofiber monoliths exhibit fully reversible H_2 sorption isotherms at 77 K and up to 100 bar, with no evidence of hysteresis. This could provide evidence that the adsorption-induced swelling of PIM-1 pores observed in N_2 sorption isotherms may not be transferrable to H_2 sorption under the same conditions of 77 K and up to 100 bar, especially that the temperature/pressure conditions lie above the critical point of H_2. It is, therefore, evident that the low-pressure H_2 uptake (P < 5 bar) follows the order, UiO-66_{powder} > UiO-66_{pellet} > UiO-66+PIM-1 > UiO-66+UiO-66/PAN-(AR), consistent with the trend observed in BET surface areas. In Table 2, the 5 bar H_2 uptake of UiO-66 pellet is 18% lower than that of UiO-66 powder, but only 9% lesser at 100 bar. Since UiO-66 has been demonstrated to be robust and remains
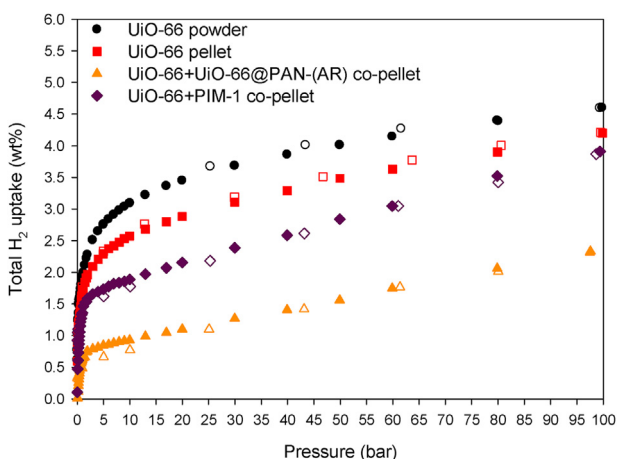

Fig. 9 — Total/absolute volumetric H_2 sorption isotherms at 77 K and up to 100 bar obtained for co-pelletized UiO-66/nanofiber monoliths. The open symbols represent desorption isotherms.

unchanged after pelletization at 700 MPa, the observed difference is explained by the slower H_2 diffusion rates into the densified UiO-66 pellet at low pressure and also by the non-equilibrium measurement conditions used during the H_2 sorption measurements. A detailed discussion of the effect of compaction/densification on H_2 uptake under non-equilibrium conditions is mentioned in our previous studies [25,26].

In the UiO-66/nanofiber monoliths, however, it is clearly evident that the 5 bar H_2 uptake was even lower in comparison to the pristine UiO-66 powder and pellet. The total 5 bar H_2 uptake of the UiO-66+PIM-1 monolith is 25% lesser in comparison to the pristine UiO-66 forms, with that of UiO-66+UiO-66/PAN-(AR) being a staggering 70% lesser in comparison to pristine UiO-66. The 100 bar H_2 uptake, on the other hand, differs in that the UiO-66+PIM-1 monolith is only 7% lesser in comparison to pristine UiO-66 pellet and that of the UiO-66+UiO-66/PAN-(AR) monolith is 55% lesser than that of pristine UiO-66 pellet. These differences clearly show that the useable gravimetric H_2 capacity of the UiO-66+PIM-1 monolith is the largest of the current series of materials, at 2.3 wt% and at least 17% higher than both pristine UiO-66 powder and pellet. This observation is supported by results in Fig. 7a, as it is evident that there is a reduction in the incremental pore volume for apertures of 13—20 Å width, in both UiO-66+PIM-1

Fig. 8 — Total/absolute gravimetric H_2 sorption isotherms at 77 K and up to 100 bar obtained for co-pelletized UiO-66/nanofiber monoliths. The open symbols represent desorption isotherms. Excess H_2 sorption isotherms are given in Fig. S10 (ESI).
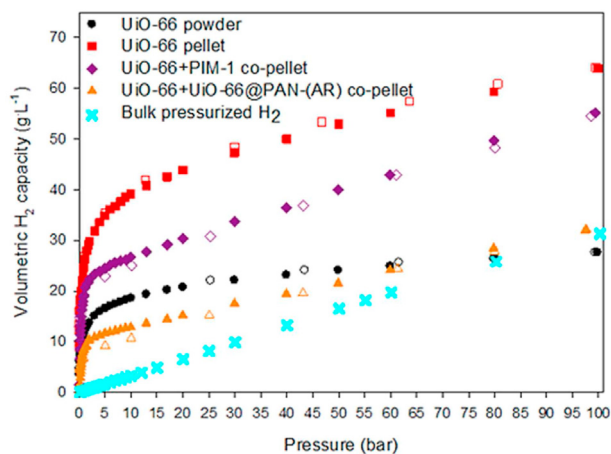
Table 4 – Total H$_2$ uptake and useable H$_2$ capacities obtained for pristine UiO-66, co-pelletized UiO-66/nanofiber monoliths, and benchmark Zn-, Al- and Zr-MOFs. The measurements were collected at a temperature of 77 K and up to 100 bar pressure.

Sample	Excess H$_2$ uptake (wt%)[a]	Total H$_2$ uptake at 5 bar[b]		Useable H$_2$ capacity[c]		Ref.
		Gravimetric (wt%)	Volumetric (g·L^{-1})	Gravimetric (wt%)	Volumetric (g·L^{-1})	
UiO-66 powder	3.1	2.8 (4.6)	18 (30)	1.8	12	[26]
UiO-66 pellet	2.5	2.3 (4.2)	35 (64)	1.9	29	[26]
UiO-66+PIM-1	2.1	1.6 (3.9)	23 (55)	2.3	32	This work
UiO-66 + UiO66/PAN-(AR)	0.8	0.7 (2.3)	10 (32)	1.6	22	This work
MOF-5 powder[d]	–	3.5 (8.0)	23.9 (55)	4.5	31.1	[56]
IRMOF-20 powder[d]	–	3.8 (9.5)	18.6 (52)	5.7	33.4	[56]
PCN-610/NU 100[d]	–	3.9 (14)	9.5 (45)	10.1	35.5	[56]
NU 1500-Al	–	8.6	46.8	8.2[e]	44.6[e]	[57]
NU 1501-Al	–	14.5	47.9	14[e]	46.2[e]	[57]

[a] Maximum measured excess H$_2$ uptake, the results may have varying pressures.
[b] Values in parentheses represent the H$_2$ uptake at 100 bar.
[c] Values calculated from the difference between total H$_2$ uptake at 100 bar (adsorption) and 5 bar (desorption).
[d] Based on measured results assuming an isothermal pressure-swing H$_2$ storage system.
[e] Usable capacities under combined temperature and pressure swing conditions of 77 K/100 bar →160 K/5 bar [57].

and UiO-66+PAN-(AR) monoliths. Due to the polymeric nature of PIM-1 and PAN nanofibers, pore blocking at the UiO-66/nanofiber interfaces can be enhanced, thereby reducing the number of adsorption sites within the aforementioned micropore region, consequently resulting in low isosteric enthalpies (heat of adsorption) typical of H$_2$ adsorption in MOFs and MOF composites, ca. 4 kJ mol^{-1} to 8 kJ mol^{-1} [7]. This affected micropore region (13–20 Å) is also attributed to the presence of defect-containing UiO-66 crystals since a defect-free UiO-66 contains apertures of 6, 8, and 11 Å as highlighted in our previous study [25]. Defects are strong H$_2$ adsorption sites in MOFs since they may be open metal sites, thereby resulting in higher heat of adsorption in the pristine UiO-66 forms in comparison to the UiO-66+nanofiber monoliths that experience pore blocking. In the UiO-66+PAN-(AR) monolith, the degree of pore blocking may be significantly greater in comparison to UiO-66+PIM-1 since the PAN nanofibers are non-porous and the PIM-1 nanofibers contain micropores with apertures of 6, 8, and 13 Å as shown in Figs. 4 and 7. Additionally, in Fig. S10 (ESI) the excess H$_2$ adsorption isotherm for UiO-66+PIM-1 monolith does not show a decrease up to 100 bar, a sign for possible adsorption-induced swelling of the PIM-1 internal porosity, thereby increasing H$_2$ uptake. In Fig. 3, the N$_2$ adsorption/desorption isotherm of the UiO-66+PIM-1 monolith also shows a large hysteresis loop, supporting the possibility of adsorption-induced pore swelling [52].

The volumetric H$_2$ capacities, in Fig. 9 and Table 4, show a different trend in comparison to the gravimetric H$_2$ capacities. The largest total volumetric H$_2$ capacity at 100 bar is obtained in the pristine UiO-66 pellet, followed by the UiO-66+PIM-1, then UiO-66+UiO-66/PAN-(AR), and lastly pristine UiO-66 powder.

The results clearly show a strong correlation of the total volumetric H$_2$ capacity to the packing density of the material, as demonstrated in our previous studies [25,26] and detailed in the work of Balderas-Xicohtèncatl et al. [8]. Interestingly, even

with the very low BET surface area and gravimetric H$_2$ capacity of the UiO-66+UiO-66/PAN-(AR) monolith, its volumetric H$_2$ capacity and most importantly the useable volumetric H$_2$ capacity exceeds that of pristine UiO-66 powder. This outcome is clearly due to the reduced low-pressure H$_2$ adsorption/uptake observed in the UiO-66+UiO-66/PAN-(AR) monolith, and gradually increasing H$_2$ uptake at moderate to high pressure (i.e. at P > 5 bar).

In Table 4, the volumetric H$_2$ capacity of the UiO-66+PIM-1 monolith is clearly lower than that of the pristine UiO-66 pellet at both 5 and 100 bar, however, the useable capacity is higher in comparison due to the low-pressure H$_2$ uptake observed in the UiO-66+PIM-1 monolith. This low-pressure H$_2$ uptake is attributed to the reduction of adsorption sites in the micropore region (13–20 Å) resulting from polymer-induced pore blocking in both UiO-66+PIM-1 and UiO-66+PAN-(AR). The presence of mesopores in the monoliths, which are absent in pristine UiO-66, is achieved by applying a simple method of co-pelletization to impart a hierarchically porous structure in UiO-66-based materials, which facilitate increasing H$_2$ uptake at moderate to high pressures (i.e. 5 bar < P ≤ 100 bar).

The comparison of the experimental results obtained in this study to two benchmark Zn-based MOFs, MOF-5 and IRMOF-20 (Isoreticular MOF-20), and an ultrahigh surface area Zr-based MOF, PCN-610/NU100, shows that the volumetric H$_2$ capacity of the UiO-66+PIM-1 monolith is higher in comparison to that of MOF-5, but lesser compared to IRMOF-20 and PCN-610/NU100. Considering the large differences in the measured BET surface areas and gravimetric H$_2$ capacities of the MOF benchmarks and PCN-610 [50], the total and useable volumetric H$_2$ capacities obtained for the UiO-66+PIM-1 monolith are competitively viable for the application of UiO-66-based MOF materials for H$_2$ applications. Furthermore, the comparison in Table 4 is based on pristine/powder forms of MOF-5, IRMOF-20, and PCN-610. The pristine MOF-5, in particular, is notoriously known for losses in

textural properties with increasing pelletization pressures, owing to the gradual loss of crystallinity as pelletization pressures are increased [5]. It would thus be expected that the UiO-66+PIM-1 monolith would outperform MOF-5 pellets compacted at 665 MPa with respect to total and useable volumetric H_2 capacities. A similar result would be expected for IRMOF-20 as it is shares topological similarities to MOF-5, however, the Zr-based PCN-610 would be expected to show little losses to textural properties and H_2 capacities upon pelletization at 665 MPa [58]. The results in this study are also compared to the impressively high gravimetric and volumetric H_2 capacities obtained onto Al-based MOFs, NU-1500-Al and NU-1501-Al, reported by Chen et. Al [57]. With the latter showing some of the highest measured useable H_2 capacities of 14 wt% (gravimetric) and 46 g L^{-1} (volumetric). Their study, however, does not report on the total and useable H_2 capacities of shaped NU-1500 and NU-1501 counterparts, and also considers conditions of combined temperature and pressure swing in comparison to isothermal pressure swing conditions reported in this study. The study by Purewal et al. [12] showed that MOFs achieve improved useable volumetric H_2 capacities under temperature and pressure swing conditions in comparison to isothermal pressure swing conditions. It can thus be expected that the useable volumetric H_2 capacities obtained in the current study would be significantly greater under temperature and pressure swing conditions than the currently reported values obtained under isothermal pressure swing conditions, and possibly comparable to that of NU-1500-Al.

Conclusion

The aim of this study was to investigate the effect of co-pelletization on the adsorption behavior of UiO-66/nanofiber monoliths in comparison to pristine UiO-66 powder and pellet forms, with particular interest in H_2 storage applications. In the co-pelletization strategy, polymer nanofibers were compressed simultaneously with UiO-66 powder at ca. 700 MPa, forming a layered monolith structure. This type of architecture is found to introduce mesopores in the monolith that are not observable in the pristine UiO-66 powder or pellet, thereby creating a monolith with a hierarchically porous structure. The results show that the typical Type I sorption isotherm of UiO-66 can be converted to a composite Type I/Type III sorption isotherm in the UiO-66+nanofiber monoliths. This hierarchical porosity enables significant reductions in low-pressure H_2 uptake (i.e. P < 5 bar), while maintaining a comparatively high H_2 uptake at moderate to high pressures (5 bar < P < 100 bar). The useable capacity of the UiO-66+PIM-1 monolith shows a considerable improvement of ca. 30%, both gravimetrically and volumetrically. For the UiO-66/nanofiber monolith containing non-porous PAN-based nanofibers, it is found that the extent of mesoporosity is enhanced and the low-pressure H_2 uptake is the lowest in comparison to pristine UiO-66 and the UiO-66+PIM-1 monolith. The significant reduction observed on monoliths with non-porous PAN nanofibers could show the importance of using porous nanofibers (with intrinsic pores or possibly fabricated onto the surface of the nanofibers) for the successful improvement of useable capacities using the proposed co-pelletization strategy. Interestingly, the difference in the useable volumetric H_2 capacity of UiO-66/nanofiber monoliths with non-porous PAN nanofibers and pristine UiO-66 powder was more than 40% but only 11% lesser than pristine UiO-66 powder in useable gravimetric H_2 capacity. The reported co-pelletization strategy, was useful for both improving the packing density of UiO-66 monoliths compared to UiO-66 powder and also impart hierarchically porous structure to improve the useable H_2 capacities of UiO-66-based MOF materials.

Declaration of competing interest

The authors declare that they have no known competing financial interests or personal relationships that could have appeared to influence the work reported in this paper.

Acknowledgements

Appendix A. Supplementary data

Supplementary data to this article can be found online at https://doi.org/10.1016/j.ijhydene.2020.12.049.

REFERENCES

[1] Ren J, Musyoka NM, Langmi HW, Swartbooi A, North BC, Mathe M. Int J Hydrogen Energy 2015;40:4617–22. https://doi.org/10.1016/j.ijhydene.2015.02.011.

[2] Rowsell JLC, Yaghi OM. Angew Chem Int Ed 2005;44:4670–9. https://doi.org/10.1002/anie.200462786.

[3] Annamalai P, Musyoka NM, Ren J, Langmi HW, Mathe M, Bessarabov D. Res Chem Intermed 2017;43:4095–102. https://doi.org/10.1007/s11164-017-2867-x.

[4] Sumida K, Liang K, Reboul J, Ibarra IA, Furukawa S, Falcaro P. Chem Mater 2017;29:2626–45. https://doi.org/10.1021/acs.chemmater.6b03934.

[5] Purewal JJ, Liu D, Yang J, Sudik A, Siegel DJ, Maurer S, Müller U. Int J Hydrogen Energy 2012;37:2723–7. https://doi.org/10.1016/j.ijhydene.2011.03.002.

[6] Farha OK, Chen Z, Wasson MC, Drout RJ, Robison L, Idrees K, Knapp JG, Son FA, Zhang X, Hierse W, Kühn C, Marx S, Hernandez B. Faraday Discuss 2020. https://doi.org/10.1039/D0FD00103A.

[7] Broom DP, Webb CJ, Fanourgakis GS, Froudakis GE, Trikalitis PN, Hirscher M. Int J Hydrogen Energy 2019;44:7768–79. https://doi.org/10.1016/j.ijhydene.2019.01.224.

[8] Balderas-Xicohténcatl R, Schmieder P, Denysenko D, Volkmer D, Hirscher M. Energy Technol 2017;6:510–2. https://doi.org/10.1002/ente.201700608.

[9] Mason JA, Veenstra M, Long JR. Chem Sci 2014;5:32–51. https://doi.org/10.1039/C3SC52633J.

[10] Furukawa H, Cordova KE, O'Keeffe M, Yaghi OM. Science 2013;341. https://doi.org/10.1126/science.1230444. 1230444–1230444.

[11] Peng Y, Krungleviciute V, Eryazici I, Hupp JT, Farha OK, Yildirim T. J Am Chem Soc 2013;135:11887–94. https://doi.org/10.1021/ja4045289.

[12] Purewal J, Veenstra M, Tamburello D, Ahmed A, Matzger AJ, Wong-foy AG, Seth S, Liu Y, Siegel DJ. Int J Hydrogen Energy 2019;44:15135–45. https://doi.org/10.1016/j.ijhydene.2019.04.082.

[13] DOE technical targets for onboard hydrogen storage for light-duty vehicles. 2020. Cited on 04 August, https://www.energy.gov/eere/fuelcells/doe-technical-targets-onboard-hydrogen-storage-light-duty-vehicles.

[14] Chapman K, Halder G, Chupas P. J Am Chem Soc 2009;131:17546–7. http://pubs.acs.org/doi/abs/10.1021/ja908415z.

[15] Ortiz AU, Boutin A, Fuchs AH, Coudert F. Phys Rev Lett 2012;109:195502. https://doi.org/10.1103/PhysRevLett.109.195502.

[16] Coudert FX. Chem Mater 2015;27:1905–16. https://doi.org/10.1021/acs.chemmater.5b00046.

[17] Rubio-martinez M, Avci-camur C, Maspoch D, Hill MR, Thornton AW, Imaz I, Rubio-martinez M. Chem Soc Rev 2017;46:3453–80. https://doi.org/10.1039/c7cs00109f.

[18] Férey G, Latroche M, Serre C, Millange F, Loiseau T, Percheron-Guégan A. Chem Commun 2003:2976–7. https://doi.org/10.1039/B308903G.

[19] Deria P, Gómez-Gualdrón DA, Bury W, Schaef HT, Wang TC, Thallapally PK, Sarjeant AA, Snurr RQ, Hupp JT, Farha OK. J Am Chem Soc 2015;137:13183–90. https://doi.org/10.1021/jacs.5b08860.

[20] Stavitski E, Pidko EA, Couck S, Remy T, Hensen EJM, Weckhuysen BM, Denayer J, Gascon J, Kapteijn F. Langumuir 2011;27:3970–6. https://doi.org/10.1021/la1045207.

[21] Wu H, Yildirim T, Zhou W. J Phys Chem Lett 2013;4:925–30. https://doi.org/10.1021/jz4002345.

[22] Rogge SMJ, Waroquier M, Van Speybroeck V. Acc Chem Res 2017;51:138–48. https://doi.org/10.1021/acs.accounts.7b00404.

[23] Balderas-Xicohténcatl R, Schlichtenmayer M, Hirscher M. Energy Technol 2017;6:578–82. https://doi.org/10.1002/ente.201700636.

[24] Zacharia R, Cossement D, Lafi L, Chahine R. J Mater Chem 2010;20:2145–51. https://doi.org/10.1039/b922991d.

[25] Bambalaza SE, Langmi HW, Mokaya R, Musyoka NM, Ren J, Khotseng LE. J Mater Chem A 2018;6:23569–77. https://doi.org/10.1039/c8ta09227c.

[26] Bambalaza SE, Langmi HW, Mokaya R, Musyoka NM, Khotseng LE. ACS Appl Mater Interfaces 2020;12:24883–94. https://doi.org/10.1021/acsami.0c06080.

[27] Xuan Z, Qingrong Z, Guobin Z, Weidong Z. Cryogenics 2020;112:103121. https://doi.org/10.1016/j.cryogenics.2020.103121.

[28] Wu H, Chua YS, Krungleviciute V, Tyagi M, Chen P, Yildirim T, Zhou W. J Am Chem Soc 2013;135:10525–32. https://doi.org/10.1021/ja404514r.

[29] Tsivion E, Veccham SP, Head-Gordon M. ChemPhysChem 2016;18:184–8. https://doi.org/10.1002/cphc.201601215.

[30] Liu Q, He P, Qian X, Fei Z, Zhang Z, Chen X, Tang J, Cui M, Qiao X, Shi Y. Energy Fuels 2017;31:13933–41. https://doi.org/10.1021/acs.energyfuels.7b02543.

[31] Amid H, Mazé B, Flickinger MC, Pourdeyhimi B. J Mater Sci 2016;51:4173–200. https://doi.org/10.1007/s10853-016-9741-x.

[32] Li S, Huo F. Nanoscale 2015;7:7482–501. https://doi.org/10.1039/c5nr00518c.

[33] Ostermann R, Cravillon J, Weidmann C, Wiebcke M, Smarsly BM. Chem Commun 2011;47:442–4. https://doi.org/10.1039/C0CC02271C.

[34] Yu L, Cebe P. Polymer 2009;50:2133–41. https://doi.org/10.1016/j.polymer.2009.03.003.

[35] Ren J, Musyoka NM, Annamalai P, Langmi HW, North BC, Mathe M. Int J Hydrogen Energy 2015;40:9382–7. https://doi.org/10.1016/j.ijhydene.2015.05.088.

[36] Lasseuguette E, Ferrari M. Mater Lett 2016;177:116–9. https://doi.org/10.1016/j.matlet.2016.04.181.

[37] Song Q, Cao S, Pritchard RH, Ghalei B, Al-muhtaseb SA, Terentjev EM, Cheetham AK, Sivaniah E. Nat Commun 2014;5:4813. https://doi.org/10.1038/ncomms5813.

[38] Lohe MR, Rose M, Kaskel S. Chem Commun 2009:6056–8. https://doi.org/10.1039/B910175F.

[39] Kapelewski MT, Runčevski T, Tarver JD, Jiang HZH, Hurst KE, Parilla PA, Ayala A, Gennett T, Fitzgerald SA, Brown CM, Long JR. Chem Mater 2018;30:8179–89. https://doi.org/10.1021/acs.chemmater.8b03276.

[40] Yang J, Sudik A, Wolverton C, Siegel DJ. Chem Soc Rev 2010;39:656–75. https://doi.org/10.1039/B802882F.

[41] Chanut N, Wiersum AD, Lee UH, Hwang YK, Ragon F, Chevreau H, Bourrelly S, Kuchta B, Chang JS, Serre C, Llewellyn PL. Eur J Inorg Chem 2016:4416–23. https://doi.org/10.1002/ejic.201600410.

[42] Roth WJ, Gil B, Makowski W, Marszalek B, Eliášová P. Chem Soc Rev 2016;45:3400–38. https://doi.org/10.1039/C5CS00508F.

[43] Vandichel M, Hajek J, Vermoortele F, Waroquier M, De Vos DE, Van Speybroeck V. CrystEngComm 2015;17:395–406. https://doi.org/10.1039/C4CE01672F.

[44] Yuan S, Huang L, Huang Z, Sun D, Qin J, Yuan S, Huang L, Huang Z, Sun D, Qin J, Feng L, Li J. J Am Chem Soc 2020;142:4732–8. https://doi.org/10.1021/jacs.9b13072.

[45] Xia K, Gao Q, Jiang J, Hu J. Carbon N. Y. 2008;46:1718–26. https://doi.org/10.1016/j.carbon.2008.07.018.

[46] Yang X-Y, Chen L-H, Li Y, Rooke JC, Sanchez C, Su B-L. Chem Soc Rev 2017;46:481–558. https://doi.org/10.1039/C6CS00829A.

[47] Connolly BM, Danaf NA, Lamb DC, Mehta JP, Vulpe D, Wuttke S, Moghadam PZ, Wheatley AEH. Nat Commun 2019:1–11. https://doi.org/10.1038/s41467-019-10185-1.

[48] Groen JC, Peffer LA, Perez-Ramirez J. Microporous Mesoporous Mater 2003;60:1–17. https://doi.org/10.1016/S1387-1811(03)00339-1.

[49] Budd PM, Msayib KJ, Tattershall CE, Ghanem BS, Reynolds KJ, Mckeown NB, Fritsch D. J Membr Sci 2005;251:263–9. https://doi.org/10.1016/j.memsci.2005.01.009.

[50] Thommes M, Kaneko K, Neimark AV, Olivier JP, Rodriguez-Reinoso F, Rouquerol J, Sing KSW. Pure Appl Chem 2015;87:1051–69. https://doi.org/10.1515/pac-2014-1117.

[51] Sing KSW, Williams RT. Adsorpt Sci Technol 2004;22:773–82. https://doi.org/10.1260/0263617053499032.

[52] Mckeown NB. ISRN Mater. Sci 2012:1–16. https://doi.org/10.5402/2012/513986.

[53] Valenzano L, Civalleri B, Chavan S, Bordiga S, Nilsen MH, Jakobsen S, Lillerud KP, Lamberti C. Chem Mater 2011;23:1700–18. https://doi.org/10.1021/cm1022882.

[54] Zhao Y, Zhang Q, Li Y, Zhang R, Lu G. ACS Appl Mater Interfaces 2017;9:15079–85. https://doi.org/10.1021/acsami.7b02887.

[55] Shearer GC, Chavan S, Ethiraj J, Vitillo JG, Svelle S, Olsbye U, Lamberti C, Bordiga S, Lillerud KP. Chem Mater 2014;26:4068–71. https://doi.org/10.1021/cm501859p.

[56] Ahmed A, Seth S, Purewal J, Wong-Foy AG, Veenstra M, Matzger AJ, Siegel DJ. Nat Commun 2019;10:1568. https://doi.org/10.1038/s41467-019-09365-w.

[57] Chen Z, Li P, Anderson R, Wang X, Zhang X, Robison L, Redfern LR, Moribe S, Islamoglu T, Gómez-Gualdrón DA, Yildirim T, Stoddart JF, Farha OK. Science 2020;368:297–303. https://doi.org/10.1126/science.aaz8881.

[58] Redfern LR, Robison L, Wasson MC, Goswami S, Lyu J, Islamoglu T, Chapman KW, Farha OK. J Am Chem Soc 2019;141:4365–71. https://doi.org/10.1021/jacs.8b13009.